

The rings of Neptune

by Imke De Pater, Stéfan Renner, Mark R. Showalter, and Bruno Sicardy

arXiv:1906.11728v1 [astro-ph.EP] 27 Jun 2019

This material has been published in *Planetary Ring Systems* (www.cambridge.org/9781107113824) edited by Matt Tiscareno and Carl Murray. This version is free to view and download for personal use only. Not for re-distribution, re-sale or use in derivative works. Cambridge University Press.

The rings of Neptune

IMKE DE PATER, STÉFAN RENNER, MARK R. SHOWALTER,
AND BRUNO SICARDY

5.1 Introduction

In 1984, three telescopes in South America recorded an occultation of a star near Neptune; since the occultation was recorded only on ingress, it was attributed to the existence of a partial ring or ring arc (Hubbard, 1986; Hubbard et al., 1986; Manfroid et al., 1986). The existence of ring arcs around Neptune was confirmed during subsequent years via other occultation experiments (Nicholson et al., 1990, 1995; Sicardy et al., 1991), and by the Voyager 2 spacecraft (Smith et al., 1989). The Voyager observations established that the Neptunian arcs are concentrations of particles embedded within Neptune’s narrow Adams ring, the outermost of six tenuous rings discovered by Voyager. Figure 5.1 shows Voyager images of the arcs in backscattered and forward scattered light. Four ring arcs were identified: the trailing arc *Fraternité*; a double-component arc *Egalité*, dubbed *Egalité 1* and *2*; *Liberté*; and the leading arc *Courage*. The arcs varied in extent from $\sim 1^\circ$ to $\sim 10^\circ$, and together were confined to a longitude range of 40° ; they had typical radial widths of ~ 15 km (Hubbard et al., 1986; Sicardy et al., 1991; Porco et al., 1995). The optical depth in the arcs is of order 0.1. Although the arcs should have been destroyed in a few months time through differential Keplerian motion, they appeared to persist at least throughout the Voyager era (Hubbard et al., 1986), and well beyond, as discussed below.

The rings discovered by Voyager (Figures 5.2, 5.3; Table 5.1) include the relatively bright and narrow Adams and Le Verrier rings, each with an optical depth of order 0.003, the faint Lassell ring (an outward extension of the Le Verrier ring), the Arago ring (the bright outer edge of the Lassell ring), and the innermost faint Galle ring. Several moderately large moons orbit within Neptune’s rings (Table 5.2); these satellites are believed to be responsible for much of the radial and longitudinal ring structure that has been observed. In addition to the above named rings, there is a sixth unnamed ring, possibly incomplete, sharing the orbit of the moon Galatea.

Since the Voyager flyby, Neptune’s rings have been observed with the Hubble Space Telescope (HST), Canada-France-Hawaii Telescope (CFHT), the Very Large Telescope (VLT), and the W. M. Keck Observatory. In the following section we will summarize the observations and analyses thereof that have been conducted since the Voyager flyby. In Section 5.3 we summarize our knowledge of the particle properties, and in Section 5.4 we review the history, sta-

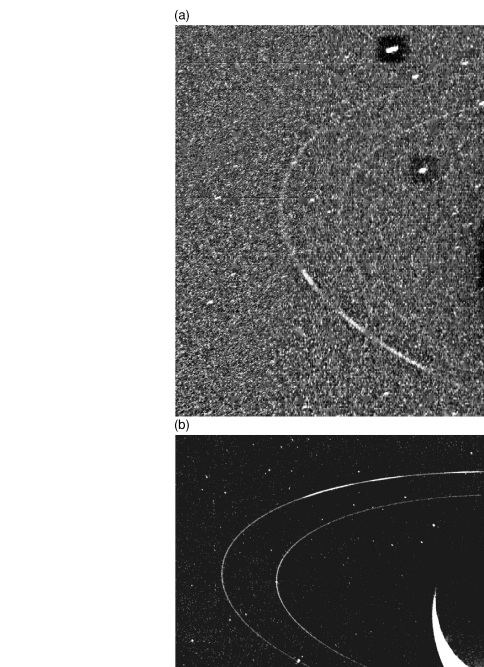


Figure 5.1 Neptune’s two most prominent rings, Adams (which includes higher optical depth arcs) and Le Verrier, as seen by Voyager 2. (a) The rings appear faint in this image, FDS 11350.23 (FDS numbers refer to the Voyager flight data system timeline. Each image has a unique FDS number), taken in backscattered light (phase angle 15.5°) with a resolution of 19 km per pixel. The moon Larissa at the top of the image appears streaked as a result of its orbital motion. The other bright object in the field is a star. The image appears very noisy because a long exposure (111 s) and hard stretch were needed to show the faintly illuminated, low optical depth dark rings of Neptune. (NASA/Voyager 2, PIA00053) (b) This forward scattered light (phase angle 134°) image, FDS 11412.51, was obtained using a 111 second exposure with a resolution of 80 km per pixel. The rings are much brighter in forward scattered light than in backscatter, indicating that a substantial fraction of the ring optical depth consists of micrometer-size dust. (NASA/Voyager 2, PIA01493)

bility, and present state-of-knowledge of the arc motions. A short review of the theories on the stability of the ring arcs is provided in Section 5.5. The chapter concludes with a summary, conclusions and outlook in Section 5.6. Chapters 12 and 13 provide background on the general physics of narrow and diffuse rings, respectively, and Chapter 13 also contains

Table 5.1. *Properties of Neptune’s ring system.*^a

	Galle	Le Verrier	Lassell	Arago	Galatea co-orbital	Adams
Radial location (Neptune radii)	1.7	2.15	2.23	2.31	2.50	2.54
Radial location (km)	42 000	53 200	55 200	57 200	61 953	62 933
Radial width (km)	2000	~100	4 000			15 (in arcs)
Normal optical depth	~10 ⁻⁴ (of dust)	~0.003	~10 ⁻⁴			0.1 in arcs 0.003 elsewhere
Dust fraction	^b	~50%	^b	^b	^b	~50% in arcs ~30% elsewhere

^a Table from de Pater and Lissauer (2015), based on data from Porco et al. (1995).^b Large particles not detected; dust fraction is likely high.Table 5.2. *Neptune’s inner (ring) moons*^a

Satellite (#ID)	a (10 ³ km)	Orbital period (days)	e	i (deg)	Radius (km)	Albedo (geometric)
III Naiad	48.227	0.294396	0.0003	4.69	33±3	0.07
IV Thalassa	50.074	0.311485	0.0002	0.14	41±3	0.09
V Despina	52.526	0.334655	0.0002	0.07	75±3	0.09
VI Galatea	61.953	0.428745	0.0001	0.03	88±4	0.08
VII Larissa	73.548	0.554654	0.0014	0.21	97±3	0.09
S/2004 N 1	105.3	0.95	unknown	unknown	9±1	0.09 (assumed)
VIII Proteus	117.647	1.122315	0.0005	0.08	210±7	0.096

^a Based on Jacobson and Owen (2004) and Jacobson (2009) and <http://ssd.jpl.nasa.gov>; the physical parameters (radius, albedo) were based on Karkoschka (2003).

a more generalized discussion of ring arcs and confinement models.

5.2 Observations since the Voyager Flyby

Images obtained with HST, the CFHT, VLT and Keck telescopes since the Voyager flyby have consistently revealed arcs in the Adams ring. In the following subsections we will summarize observations at near-infrared and at visible wavelengths, and present the evolution over time of the ring arcs. To facilitate comparison between different data sets, we typically calculate the equivalent width, EW , in meters: $EW = \int (I/F) dr$, where I is the observed intensity, πF is the solar intensity arriving at Neptune at the particular wavelength, and r is distance across the rings. The equivalent width is thus the equivalent extent of a ring (in meters) if the ring had a reflectivity $I/F = 1$ (i.e., a perfect Lambertian reflector).

5.2.1 Near-Infrared Observations

The first post-Voyager images of Neptune’s ring arcs were obtained with the Near Infrared Camera Multi-Object Spectrograph (NICMOS) on HST (Dumas et al., 1999) at 1.87 μm and from the ground with the CFHT (Sicardy et al., 1999) at 1.72 μm , both in 1998. To minimize scattered light

from Neptune, one ideally observes the rings at wavelengths that correspond to methane absorption bands. Light from Neptune itself is suppressed most at 1.8–2.2 μm , due to both absorption by methane gas and collision induced absorption by hydrogen gas in the planet’s atmosphere. Although methane absorption bands are less strong at shorter wavelengths (e.g., 1.6 vs 2.1 μm), solar radiation is stronger, and hence it is not entirely clear which wavelength bands are best suited to detect Neptune’s rings.

None of the continuous rings were recovered in the HST/NICMOS images, but the ring arcs were. In order to build-up sufficient signal-to-noise in any ground-based or HST near-infrared image to identify and characterize the arcs, a large number of images need to be combined. Due to the keplerian orbital motion of moons and ring arcs around the planet, any co-adding of frames, or long integration times, leads to a smearing of moons and ring arcs. Fig. 5.4a, integrated over 832 s, is smeared over 8° in longitude, which corresponds roughly to the full length of the longest arc, *Fraternité*. Hence, in order to get a crisp image of the ring arcs, the images need to be manipulated such as to take out the orbital motion of the ring arcs. Fig. 5.4b is composed of 22 individual images, each integrated over 208 s. Each image was reprojected such that the system is viewed from above, i.e., along the ring-plane normal, and rotated such that the arcs remained fixed in position. The smearing effect was thus reduced by a factor of 4 compared

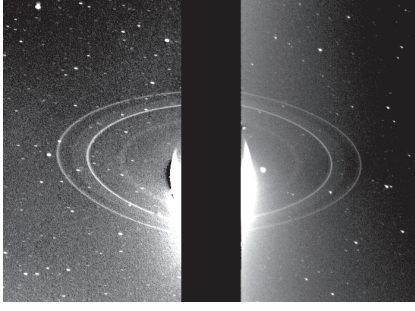


Figure 5.2 These two 591-second exposures of the rings of Neptune were taken with the clear filter by the Voyager 2 wide-angle camera on Aug. 26, 1989 from a distance of 280,000 km. The two main rings (Le Verrier and Adams) are clearly visible and appear complete over the region imaged. The time between exposures was one hour and 27 minutes. [During this period the bright ring arcs were on the opposite side of the planet for each exposure, such that they are not shown here.] Also visible in this image is the inner faint ring (Galle) at about 42,000 km from the center of Neptune, and the faint band (Lassell) that extends smoothly outward from the Le Verrier ring to roughly halfway between the two bright rings. Both of these rings are broad and much fainter than the two narrow rings. These long exposure images were taken while the rings were back-lighting by the sun at a phase angle of 135° . The bright glare in the center is due to over-exposure of the crescent of Neptune. (PIA01997)

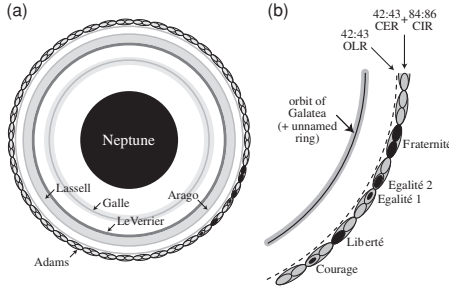


Figure 5.3 Cartoon sketch of Neptune's rings and associated moons as viewed from the south pole showing: (a) the location and names of the main rings; (b) a model for the arcs in the Adams ring (as it appeared when Voyager 2 encountered Neptune in 1989); the arcs are shown as filled centers of libration of the Galatea's 42:43 corotation eccentricity resonance (CER) and 84:86 corotation inclination resonance (CIR). The location of the two resonances (CER+CIR) as shown in the figure is not that of the nominal CIR but that of the observed arc mean motion. See Sections 5.4 and 5.5 for details on resonances. (Figure from de Pater and Lissauer (2015); Courtesy Carl Murray)

to the image in panel a. In this composite image the ring arcs are clearly visible.

In July 2002 and October 2003 the system was imaged using the near-infrared camera NIRC2 with the adaptive optics (AO) system on the 10-m Keck telescope at wavelengths of $1.6 \mu\text{m}$ and $2.12 \mu\text{m}$ (de Pater et al., 2005). An example of one of their composite images is shown in Figure 5.5. Each individual image was integrated over 60 sec, so that longitudinal smearing was minimized: i.e., in 60 sec the ring arcs are smeared by $\sim 0.6^\circ$ longitude, which corresponds to

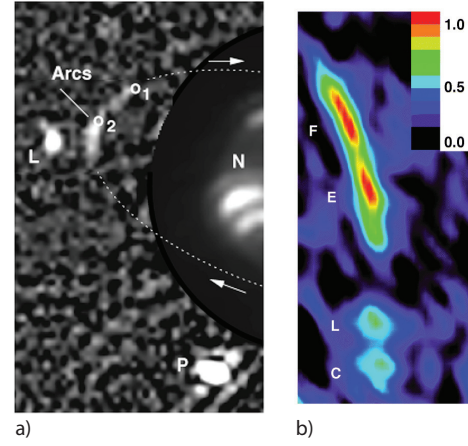


Figure 5.4 Images of Neptune's ring arcs obtained with HST/NICMOS at $1.87 \mu\text{m}$ in 1998. a) a single 832-s image, where Neptune's disk was positioned partly outside the camera's field of view to reduce its scattered light. Neptune's contribution to the background had been modeled and removed. An image of Neptune's clouds has been superimposed for better clarity of the system geometry. The two circles (labeled 1 and 2) correspond to the positions of the middle-point of the trailing arc Egalité derived from two possible solutions for the arcs' mean motion: $820.1194^\circ/\text{day}$ and $820.1118^\circ/\text{day}$ (Section 5.4). The letters L, P, and N mark the positions of Larissa, Proteus, and Neptune, respectively, and the arrows show the direction of motion of the ring arcs along their orbit. b) Composite false-color image of Neptune's ring arcs, constructed from a total of 22 dithered images, 208 s each, obtained in June and October 1998 (see text for details). The letters C, L, E and F indicate, from leading to trailing, the respective location of the arcs Courage, Liberté, Egalité and Fraternité. The intensity scale has been normalized to unity. (Figure from Dumas et al. (1999))

$\sim 0.035''$ (or less, depending on geometry) on the plane of the sky, which is less than the angular resolution of the Keck telescope ($\sim 0.05''$). The authors typically took 5 images in rapid succession. The bright short arcs in Fig. 5.5 are produced by the motion of the satellites during this sequence of 5 images. Both the complete Adams and Le Verrier rings are visible in this image, which had been integrated over a total of 30 min. Figure 5.6 shows a radial profile through the ring system (in red), compared to a radial profile from the Voyager data (black). The Keck profile is extracted from the 2002 and 2003 data, where on each day a radial profile was constructed from a composite image like that displayed in Fig. 5.5, by averaging the data in longitude away from satellites and ring arcs. The profile shown is an average of all profiles. Whereas groundbased measurements of the neptunian system are always near zero degree phase angle, the Voyager data in Fig. 5.6 were taken at a phase angle of 135° , highlighting dust. The brightness contrast between the Le Verrier and Adams rings is very similar in the Keck and Voyager data, despite the very different wavelengths and phase angles. This provides support that both rings have similar particle properties, as had been suggested based on the Voyager phase curves (Showalter and Cuzzi, 1992; Porco et al., 1995).

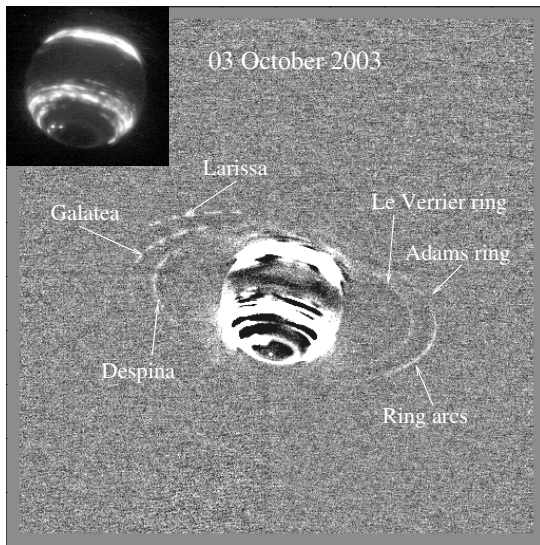


Figure 5.5 Composite image constructed from data obtained with the Keck telescope at $2.12 \mu\text{m}$ on 3 October 2003, revealing satellites, ring arcs and the complete Adams and Le Verrier rings. The image has been high-pass filtered by subtracting the same image median-smoothed with a width of 50 pixels (1 pixel = $0.01''$). This procedure removes diffuse scattered light, and brings out small-scale features (Neptune is highly saturated in this presentation). A 1-minute exposure of Neptune itself at $2.12 \mu\text{m}$ is shown in the insert. (Figure from de Pater et al. (2005))

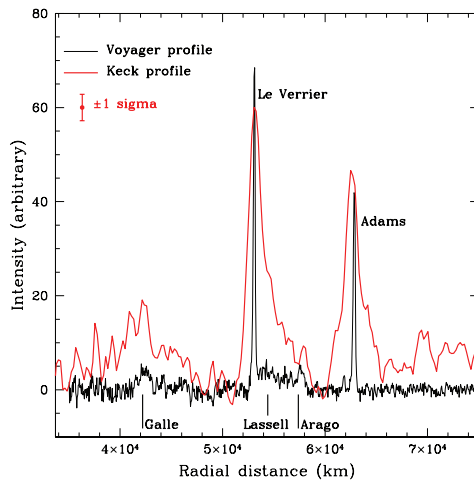


Figure 5.6 Radial profiles through the rings. The profiles in red were extracted from the Keck observations in 2002 and 2003, by averaging over azimuth on each day (i.e., on images like that displayed in Fig. 5.5), away from satellites and ring arcs, and then averaging the profiles. The black profile is from the Voyager data. The intensity scale is in arbitrary units, and the peak intensities of the Keck profile were scaled to those of the Voyager profile. (Figure from de Pater et al. (2005))

To image the individual arcs, de Pater et al. (2005) corrected for the arcs' differential motion by “unfolding” the arcs along their orbits, i.e., create images where the y-axis is along the radial direction (i.e., from the arc to the center of planet) and the x-axis is along the azimuthal (orbital) direction. After shifting and adding all 51 images from July

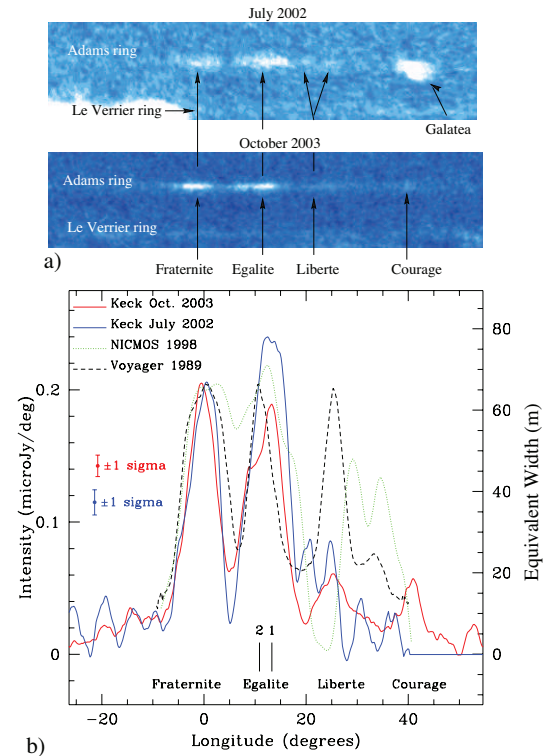


Figure 5.7 a) Reprojected image of the ring arcs from July 2002 and October 2003. b) Longitudinal scans through the ring arcs as seen by Keck, Voyager (1989) and NICMOS (1998). The Keck and Voyager profiles were smoothed to a resolution of 3° . All intensities are scaled to that of Fraternité in October 2003. Equivalent width (in m) is shown on the right. Zero longitude was chosen to coincide with the center of arc Fraternité. (Figure from de Pater et al. (2005))

2002, and, separately, the 93 images obtained from October 2003, high signal-to-noise images of the ring arcs were created, which are displayed in Figure 5.7a. Longitudinal scans through these images are shown in panel b, where the data were integrated over the arcs in the radial direction. Although the intrinsic longitudinal resolution is of order 0.5° , the curves were smoothed to a longitudinal resolution of 3° for better comparison with the Voyager and HST/NICMOS data. Equivalent width (in m) is shown on the right, scaled to the approximate intensity of arc Fraternité in 2003. The approximate location of the various arcs, including the positions of the two subregions, 1 and 2, of arc Egalité, are indicated. The zero-degree longitude was chosen to coincide with the center of arc Fraternité. This figure shows that the two leading arcs were slowly fading away, and Courage had jumped $\sim 8^\circ$ ahead in its orbit by 2003, which corresponds to one full resonance site out of 43 sites (see Sections 5.4, 5.5 for explanations on resonance sites). The intensity of Egalité, and the relative intensity of its two components, varied somewhat as well.

Renner et al. (2014) used the AO-fed camera NACO at the VLT to image the Neptunian system in August 2007 at a wavelength of $2.2 \mu\text{m}$. To enhance the signal-to-noise of ring arcs, they reprojected the rings in a similar way as

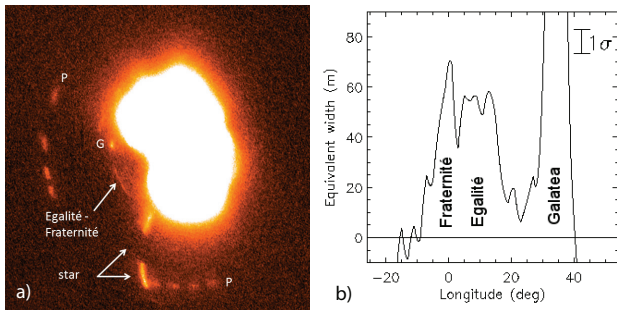


Figure 5.8 a) Projected and co-added VLT images of Neptune's equatorial plane (August 2007, 60 min total exposure time), revealing material at the Fraternité and Egalité locations and the satellites Proteus (P) and Galatea (G). Image dimension is 16.4 arcsec². b) Longitudinal scan through the ring arcs from panel a, integrated over the ring width. (Figure from Renner et al. (2014))

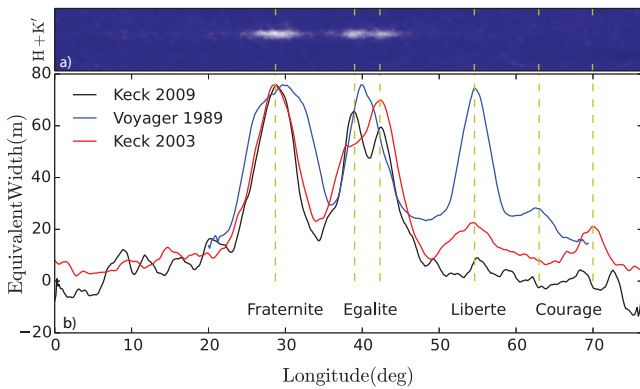


Figure 5.9 a) Deprojected image of the ring arcs from July 2009. Data at 1.63 μm (H band) were combined with data at 2.12 μm (Kp band). b) Longitudinal scans through the ring arcs as seen by Voyager in 1989, and Keck in 2003 and 2009. The Keck and Voyager profiles were smoothed to a resolution of 3°. All intensities are scaled to that of Fraternité in October 2003. (Unpublished data; figure courtesy Patrick Fitzpatrick and Imke de Pater.)

was done with the HST/NICMOS data. Their final image, viewed from above, is shown in Fig. 5.8a. A longitudinal scan through the ring arcs is shown in panel b.

Figure 5.9 shows the ring arcs as they appeared in July 2009, in observations obtained with the Keck telescope at 1.63 μm and 2.12 μm ; the data at these two wavelengths were combined to produce this image and the scans. The data reduction and analysis followed that of de Pater et al. (2005). The data were scaled to the arc Fraternité in 2003.

While no change in Fraternité's EW can be discerned between 2003 and 2007 ($\sim 65\text{--}70$ m) (Renner et al., 2014), over the years the relative intensity of most ring arcs changed dramatically. Compared to arc Fraternité, Egalité changed both in relative brightness and longitudinal extent since the Voyager flyby. In 2002 Egalité was $\sim 17\%$ brighter than Fraternité, in 2003 its intensity decreased to $\sim 7\%$ below that of Fraternité, and in 2007 and in 2009 it was $\sim 20\%$ fainter than Fraternité. The relative brightness between ring arcs Egalité 1 and 2 also changed over the years. We further note that

while Egalité has increased in overall longitudinal extent, Fraternité decreased by $\sim 25\%$ compared to that observed by Voyager (de Pater et al., 2005).

HST/NICMOS and Keck observations revealed that arc Liberté decreased in intensity since the Voyager flybys. In 1998 the arc's intensity (relative to Fraternité) had decreased by $\sim 25\%$, and it was observed $\sim 3^\circ$ ahead in longitude. In 2002, Liberté may have split into two narrow arcs, separated by $\sim 4.5^\circ$, with the leading arc at the original Voyager location. After smoothing the profile to the approximate angular resolution of the NICMOS data (Fig. 5.7), the two arcs resemble the double-hump structure observed by NICMOS; however, the NICMOS profile consists of the two arcs Liberté and Courage (Dumas et al., 1999), whereas in 2002 the Keck double-hump curve is just Liberté. In 2003, Liberté appears again as one arc at the original Voyager (1989) location, but at just $\sim 30\%$ of its original brightness.

Courage, usually a low-intensity arc, flared in intensity to become nearly as bright as Liberté when NICMOS observed it in 1998; this flaring was attributed at the time to a possible exchange of material between the two arcs. In 2003, both Courage's and Liberté's intensities had decreased to levels comparable to those of Courage's intensity in 1989. Interesting is Courage's apparent $\sim 8^\circ$ shift in the leading direction in 2003 compared to the Voyager era. If Courage was also 8° ahead in its orbit in 2002, it would have been hidden by bright Galatea, which was very close to the ring arcs at that time (Fig. 5.7a). Unfortunately, Galatea also interfered with the two leading arcs at the time of the VLT observations in 2007, and hence no unambiguous information on Courage nor Liberté can be derived (Fig. 5.8). By 2009, both Liberté and Courage have essentially disappeared (Fig. 5.9).

5.2.2 Visible-light Observations (HST)

Because of the intense glare from Neptune when observing outside methane absorption bands, only the Hubble Space Telescope (HST) is able to study Neptune's inner rings and moons at visual wavelengths. These observations have the advantage, however, that they cover wavelengths very similar to those from Voyager in 1989, making direct photometric comparisons possible. This in spite of the fact that the highest phase angle observable from Earth, 1.9° , is well below the minimum phase angle of $\sim 8^\circ$ observed by Voyager.

Typical HST observations of the Neptune system have focused on the planet itself, using relatively short exposures. These are useful for atmospheric studies but are inadequate to detect the rings, arcs and small moons. Long exposures, in which the planet itself saturates, are required. Such images of the Neptune system were obtained by HST's Advanced Camera for Surveys in 2004–2005 (Showalter et al., 2005) and by the Wide Field Camera 3 (WFC3) in 2009 (Showalter et al., 2013b). The analysis of a similar 2016 data set is not yet complete (Showalter et al., 2016).

The HST observations have been notable for a few reasons that may or may not be related to the rings. For one, these data revealed a small moon, S/2004 N 1, orbiting between Larissa and Proteus (Showalter et al., 2013a). Indications so far are that this moon was too small to have been

Table 5.3. *Reflectivities of Galatea and the Ring Arcs*

	Voyager ^a 0.5 μm	NICMOS ^b 1.87 μm	Keck 2002 ^c 2.12 μm	Keck 2003 ^c 2.12 μm	Keck 2003 ^c 1.63 μm
Galatea I/F ^d	0.079	0.086 ± 0.06	0.096 ± 0.015	0.094 ± 0.011	0.088 ± 0.012
Arcs (F+E) I/F ^d	0.055 ± 0.004	0.083 ± 0.012		0.088 ± 0.012	0.082 ± 0.013

^a Porco et al. (1995); Karkoschka (2003); ^b Dumas et al. (1999); ^c de Pater et al. (2005). ^d Assumed: 15 km radial extent; 25° in azimuth; normal optical depth $\tau = 0.1$ (Porco et al., 1995). The NICMOS reflectivity is for the entire ring arc system.

detected by Voyager’s cameras. Furthermore, they have revealed that Naiad, the innermost known moon, has deviated substantially from its predicted orbit. Whether this reveals the influence of some hitherto unknown perturbation, or is just the result of ephemeris uncertainty, is not yet known.

The arcs show up clearly in these images, as do the Le Verrier and Adams rings. As was also noted in the infrared studies (Fig. 5.9), the leading arcs have dissipated and can no longer be seen. The two trailing arcs, Egalité and Fraternité, remain, although they appear to have narrowed slightly. Careful photometry suggests that they are diminished in brightness relative to the Voyager flyby in 1989.

5.3 Particle Properties

Imaging, occultation and *in situ* data can be used to derive particle properties of Neptune’s rings. The premier data set to determine such properties is the Voyager data set, because it is the only one where both low- and high-phase angle data have been obtained. Particle properties as derived from the Voyager data have been reviewed in detail by Porco et al. (1995). The particles in Neptune’s rings are very dark, perhaps as dark as the particles in the uranian rings. The fraction of optical depth due to micrometer-sized dust is very high, $\sim 50\%$, and appears to vary from ring to ring. The limited data available are not sufficient to make even an order-of-magnitude estimate of the mass of Neptune’s rings, although the data suggest that the rings are significantly less massive than the rings of Uranus, unless they contain a substantial population of undetected large ($\gtrsim 10$ m) particles, which is unlikely given the paucity of smaller macroscopic ring particles.

Since the Voyager flyby, the data base has been extended by groundbased near-infrared (5.2.1) and visible light HST data (5.2.2). Table 5.3 summarizes measured reflectivities for Galatea and the ring arcs. As shown, Galatea has a slight red color, whereas the ring arcs are very red. A red color is typical for dusty rings, such as Jupiter’s rings (de Pater et al., 1999), Saturn’s G ring (de Pater et al., 2004), and the ν ring of Uranus (de Pater et al., 2006).

5.4 Motion of the Arcs

Nicholson et al. (1995) analyzed the Voyager images together with ~ 25 stellar occultations by the Neptune system which were observed from Earth-based telescopes between 1984 and 1988. All observations combined indicated a mean orbital motion of the arcs of either $820.1194 \pm 0.0006^\circ/\text{day}$ (referred to as solution 1) or $820.1118 \pm 0.0006^\circ/\text{day}$ (referred to as solution 2). Solution 1 appeared to be consistent with the value that was expected if the arcs are in a 42:43 corotation inclination resonance (CIR) with nearby satellite Galatea, a model suggested soon after the arcs were first discovered in occultation profiles (Goldreich et al., 1986), and attributed to the neptunian system after the Voyager flybys by Porco (1991).

Galatea’s average mean motion is $n_G = 839.66129 \pm 0.00002^\circ/\text{day}$. The mean motion of the 42:43 CIR with Galatea, n_{CIR} , creates 86 equally spaced corotation sites around Neptune, which are located at potential maxima. The CIR mean motion is given by $n_{CIR} = (42n_G + \dot{\Omega}_G)/43$, where $\dot{\Omega}_G$ is Galatea’s nodal precession rate. Using $\dot{\Omega}_G = -0.714836^\circ/\text{day}$ (Owen et al., 1991), $n_{CIR} = 820.11760 \pm 0.00008^\circ/\text{day}$, where the uncertainty is caused by that on Galatea’s mean motion (Renner et al., 2014).

Since Voyager, the ring arcs were imaged with HST/NICMOS (Dumas et al., 1999) and from the ground with CFHT (Sicardy et al., 1999), both in 1998. Dumas et al. (2002) derived a mean motion of $820.1122 \pm 0.0003^\circ/\text{day}$ for the arcs from the HST data, and Sicardy et al. (1999) derived a value of $820.1135 \pm 0.0009^\circ/\text{day}$ from the CFHT data. Using the Keck data taken in 2002 and 2003, de Pater et al. (2005) derived a value of $820.1118 \pm 0.0001^\circ/\text{day}$, and Renner et al. (2014) determined a value of $820.11213 \pm 0.00008^\circ/\text{day}$ from VLT data taken in 2007. Showalter et al. (2013b) obtained an almost identical value, $820.1121 \pm 0.0001^\circ/\text{day}$, from HST/WFC3 observations. Clearly, the motion of the ring arcs appears to be inconsistent with the value expected if the arcs are confined by the above-mentioned 42:43 CIR.

The drift in mean motion between the CIR and the arcs is $\Delta n = n_{CIR} - n_{arcs} = (5.5 \pm 0.1) \times 10^{-3}^\circ/\text{day}$, equivalent to a mismatch $\Delta a \simeq 300 \pm 5$ m in semi-major axis (Renner et al., 2014). This drift translates into a $\simeq 36 \pm 0.7^\circ$ difference for the arcs’ longitude over the 18 years between the Voyager and 2007 VLT data. Given that all measured values for n_{arc} are essentially equal within their errorbars, it is clear that the stability of the arcs cannot be explained with the CIR model.

In the following Section we will review the theory how to stabilize the arcs, and discuss the implications for Neptune's arcs.

5.5 Stability of Arcs

5.5.1 Resonant confinement

5.5.1.1 Spreading of a free Keplerian arc

Stable ring-arcs are *a priori* fragile structures, as they must resist both radial and azimuthal spreading. Free arc particles moving along Keplerian orbits spread azimuthally at a rate

$$\delta n = -\frac{3}{2}n\frac{\delta a}{a}, \quad (5.1)$$

where δn is the difference in mean motion for a set of ring particles with a spread δa in the semi-major axes, and where n and a are the mean orbital angular frequency and the mean ring semi-major axis, respectively. The corresponding spreading timescale is

$$T_S = \frac{2\pi}{|\delta n|} = \frac{4\pi}{3\sqrt{GM}} \frac{a^{5/2}}{\delta a}, \quad (5.2)$$

using Kepler's third law $a^3 n^2 = GM$.

Thus, Neptune's ring arcs would be completely destroyed on a timescale $T_S \simeq 3.4$ years, using $a = 62932.7$ km (Rennert et al., 2014), $GM = 6.8351 \times 10^6$ km³ s⁻² (Owen et al., 1991), and assuming that the radial width of the arcs, $W \simeq 15$ km (Hubbard et al., 1986; Sicardy et al., 1991; Porco et al., 1995), is equal to the semi-major axis dispersion δa . Actually, the Keplerian shear in a ring of width $W \simeq 15$ km and mean mean motion $n = 820.11213^\circ/\text{day}$ (Rennert et al., 2014) implies $\delta n \simeq -0.29321^\circ/\text{day}$, i.e. a lengthening of the arcs of about $0.3^\circ/\text{day}$. Such a large value should have been detected by the observations, thus showing that the arcs must be actively confined.

All the arc models proposed so far essentially rely on the notion of corotation resonances (see Chapters 11 and 13). An archetype of it is the co-orbital (or 1:1) mean motion resonance, in which the two triangular Lagrange points L_4 and L_5 offer dynamically stable points around which particles can librate. The main problem with the Lagrange points, however, is that they correspond to local maxima of energy, and are therefore unstable against inter-particle, dissipative collisions.

Near a $m+1:m$ Mean Motion Resonance (MMR), there are actually two coupled resonances, one of corotation type (eccentric or inclined) and one of eccentric Lindblad type, see more details below, as well as in Foryta and Sicardy (1996) and El Moutamid et al. (2014). In that context, the same satellite can at the same time create the corotation sites where the arcs are azimuthally confined, and provide the energy necessary to counteract the effect of dissipative collisions, thus confining the arcs radially. This coupling is described in more detail in the next subsection.

5.5.1.2 Corotation vs. Lindblad resonances

In the restricted three-body problem (a massless particle perturbed by a satellite), a corotation resonance occurs at a radial location where the particle's mean motion n equals the pattern speed Ω_p of a perturbing potential. Such a resonance excites periodic variations in semi-major axis a and in longitude λ , leading to slow librations around equilibrium points. In the frame rotating at angular velocity n , the particle guiding center has a pendulum-like motion along a closed loop that surrounds one of the equilibrium points. This loop is enclosed into a separatrix, which defines a so-called corotation site.

In the example of the Lagrange points L_4 and L_5 mentioned earlier, the pattern speed is simply the mean motion of the perturbing satellite, n_S . However, a satellite moving on an eccentric or inclined orbit creates additional corotation resonances located outside its own orbit. The strongest of them correspond to first order MMRs and have pattern speeds Ω_p that satisfy:

$$m\Omega_p = (m+1)n_S - \dot{\varpi}_S, \quad (5.3)$$

or

$$m\Omega_p = (m+1)n_S - \dot{\Omega}_S, \quad (5.4)$$

where $\dot{\varpi}_S$ and $\dot{\Omega}_S$ are the apsidal and nodal satellite precession rates, respectively. These two equations define, through $n = \Omega_p$, the Corotation Eccentric Resonance (CER) and the Corotation Inclined Resonance (CIR), respectively. For instance a CER corresponds to $n = \Omega_p = n_S + \kappa_S/m$, where $\kappa_S = n_S - \dot{\varpi}_S$ is the satellite epicyclic frequency. Then, the mean motion of the particle matches the pattern speed Ω_p of the perturbing potential, hence the denomination corotation. Finally, it can be shown that the CER creates m corotation sites where arcs can potentially be maintained, while the CIR creates $2m$ sites (Goldreich et al., 1986).

To first order in e , the particle motion can be described as the superposition of an epicyclic motion of radial amplitude ae and frequency κ around a guiding center that moves uniformly at frequency n along a circular orbit with radius a . The epicyclic frequency κ and the mean motion n are related by $\kappa = n - \dot{\varpi}$, where $\dot{\varpi}$ is the particle apsidal precession rate.

The strongest (first order) Lindblad Eccentric Resonances (LERs) occur at radial locations where:

$$mn = (m+1)n_S - \dot{\varpi}, \quad (5.5)$$

or equivalently

$$\kappa = (m+1)(n - n_S). \quad (5.6)$$

Then, the epicyclic frequency is a multiple integer of the difference between the particle's mean motion n and the pattern speed, here $\Omega_p = n_S$, of the perturbing potential.

The quantity $n - n_S$ is the synodic frequency, i.e. the frequency at which the satellite is in conjunction with the particle and perturbs it through periodic tugs in the radial direction. The relation $\kappa = (m+1)(n - n_S)$ shows that at a LER, the free epicyclic frequency of the particle matches one harmonic of the radial forcing due to the satellite. Consequently, the LER excites the particle orbital eccentricity

e. This is in fact the source of energy that the particles need to balance the effect of dissipative collisions.

For $m \gg 1$, each corotation resonance is situated very near a Lindblad resonance of the same satellite. Considering first the case where the particle is trapped in a CER and perturbed by the associated LER, we have, from Eqs. (5.3) and (5.5):

$$n_{CER} - n_{LER} = \frac{\dot{\varpi} - \dot{\varpi}_S}{m}. \quad (5.7)$$

We use here the approximate expression $\dot{\varpi} \simeq 3n(R/a)^2 J_2/2$ for the particle precession rate (with similar expression for the satellite), where R and J_2 are respectively the radius and the dynamical oblateness of the central planet. Thus:

$$a_{LER} - a_{CER} \simeq \frac{2}{3} \frac{a}{n} (n_{CER} - n_{LER}) \simeq J_2 \left(\frac{R}{a} \right)^2 \frac{4a}{3m^2}, \quad (5.8)$$

which shows that the CER is always *inside* the LER, regardless of the position of the particle with respect to the satellite orbit (i.e. regardless of the sign of m).

The same kind of exercise for a particle trapped in a CIR and perturbed by the associated LER yields:

$$a_{LER} - a_{CIR} \simeq J_2 \left(\frac{R}{a} \right)^2 \frac{2a}{m}. \quad (5.9)$$

The situation is different from the previous case: the LER is now always *between* the CIR and the satellite orbit.

The relative position of the corotation and Lindblad resonances is an important ingredient for the arc confinement. As discussed in Section 5.5.4, the energy transfer from the LER actually depends on the gradient of torque from the satellite, whose sign depends in turn on the position of the LER with respect to the corotation resonance.

We now review the different models for the arcs' confinement that have been developed to account for the available observations.

5.5.2 Arcs maintained by corotation resonances of a single satellite

Goldreich et al. (1986) built up the most economical model for the arcs, requiring only one satellite that perturbs the arcs through a $m+1:m$ first order MMR, as described in Section 5.5.1.2. A satellite on an inclined orbit rather than eccentric was originally proposed, because the eccentricity is more efficiently damped due to tidal effects. The perturbing potential arising from the corotation resonance is

$$\Phi_{CIR} = -i_m^2 A_{CIR} \cos \Psi_{CIR} \quad (5.10)$$

where

$$A_{CIR} = \frac{M_S}{M_P} n_S^2 a_S^2 V, \quad (5.11)$$

$$V = \frac{\beta^2}{8} b_{3/2}^{(2m+1)}(\beta), \quad (5.12)$$

i_m is the relative inclination between the satellite and ring orbits, Ψ_{CIR} is the CIR resonance argument, $b_{3/2}^{(2m+1)}$ is a Laplace coefficient (Murray and Dermott, 2000), and $\beta = a/a_S$.

Table 5.4. *42:43 Resonances^a with Galatea.*

Type	Location (km)	Width (km)
42 : 43 CIR	62932.48 \pm 0.13	0.6
42 : 43 LER	62930.83 \pm 0.13	9

^a From Porco (1991).

Porco (1991) used the high resolution images from the Voyager spacecraft to determine accurately the arcs' radial position, and explain their stability thanks to the resonant perturbations attributable to the nearby satellite Galatea. Porco (1991) applied the model of Goldreich et al. (1986) and argued that the arcs are confined by a 42 : 43 CIR with this moon¹, using the mean motion of the arcs ($820.1185 \pm 0.0004^\circ/\text{day}$) derived by Nicholson et al. (1990). More precisely, the location of the 42 : 43 CIR was coincident with the value of the semimajor axis ($a = 62932.37 \pm 0.02$) inferred from the arcs' mean motion, considering the uncertainties and the CIR resonance width (see Table 5.4). The Voyager data also indicated that the arcs have a radial distortion of amplitude 29.6 ± 1.5 km, compatible with the eccentricity forcing of the ring particles ($e_f = (4.7 \pm 0.2) \times 10^{-4}$) due to the associated 42 : 43 LER, whose location falls 1.5 km interior to the ring's centerline (Table 5.4). Porco (1991) verified that the longitude at epoch of conjunction between Galatea and the ring particles coincides with the longitude of the satellite, as expected if all of the particle orbits are exterior to the LER resonance. The mass of the satellite Galatea could be estimated from the observed forced eccentricity: $M_G = 2.12 \pm 0.21 \times 10^{18}$ kg. Utilizing measurements of Galatea's size obtained from Voyager image analysis (Thomas and Veverka, 1991), one obtains a density of $\rho_G = 1.0 \pm 0.5 \text{ g.cm}^{-3}$, a result falling within the range of reasonable densities expected in the Neptune system.

If the arcs are within the corotation sites of Galatea's 42:43 CIR, then one might expect them to have azimuthal lengths less than $360/2|m| = 4.1860^\circ$. The Voyager brightness profiles showed that the arcs Courage, Liberté and Egalité approximately meet this criterion, but not Fraternité, whose angular extent was 9.6° . The arc separations are also not exact integer multiples of 4.1860° . Smith et al. (1989) and Porco (1991) suggested that bigger bodies, sources of the observed dust material, may librate in the corotation sites and alter the position of the arcs.

The CIR resonance width ($W_{CIR} \simeq 0.6$ km) is much smaller than the observed width of the ring arcs (15 km). A low spread in semimajor axis Δa is compatible with the coherent radial distortion observed through the ring. Otherwise, with e.g. $\Delta a \gtrsim 2$ km, the ring particles would be located on either side of the Lindblad resonance, the orbits with $a > a_{LER}$ and $a < a_{LER}$ would be shifted by π , and therefore the radial excursion would not be coherent. On the other hand, if we assume that the spread in particle semimajor axes is equal to the resonance width, $\Delta a = W_C$, then all particles would have $a > a_{LER}$, their perturbed

¹ The resonance argument is $\Psi_{CIR} = 2[43\lambda - 42\lambda_G - \Omega_G]$, where λ and Ω are respectively the mean longitude and the longitude of the ascending node, and the subscript G denotes Galatea.

orbits would all be in phase, and the spread in their forced eccentricities, Δe_f , due to their differing distances from the Lindblad resonance would yield a ring whose width would vary from W_C at quadrature (where the particle orbits cross) to $a\Delta e_f$, which can be as large as the observed width of the arcs. Then the arcs have more likely a radial width which results from the spread in eccentricity.

The Porco (1991) model required revision after post-Voyager observations showed that the arcs' motion is not consistent with the value corresponding to the CIR (Section 5.4), Namouni and Porco (2002) showed how the 42:43 CER² can match the current arcs' semi-major axis and stabilize the system, if the arcs have a sufficient fraction of the mass of Galatea. This resonance creates 43 potential maxima, each of length 8.37° , which does not completely account for the angular lengths of the arcs. The ring mass determined to shift the CER to the arcs' position, $\simeq 0.002$ Galatea's mass, assumes an eccentricity of 10^{-6} for Galatea and would correspond to a small satellite of 10 km in radius, for a density of $\simeq 1 \text{ g.cm}^{-3}$. The mass required in this model cannot be contained in a single body since Voyager data excluded undetected satellites of radius larger than 6 km (Smith et al. (1989); Porco et al. (1995)). The exact origin of the small residual orbital eccentricity of Galatea, consistent with a forcing by Adams ring's small mass, has to be determined too.

5.5.3 Stability by co-orbital moonlets

An alternative solution is to assume that the Adams ring is a collection of a few moonlets that maintain stable co-orbital relative positions akin to the Lagrangian L_4/L_5 points (Renner and Sicardy, 2004). The observed arcs would then be composed of dust trapped between those co-orbital satellites, an intermediate situation between a fully collisional ring with only small particles, and a fully accreted system of only one satellite. This generalizes the original shepherd-ing model proposed by Lissauer (1985) and is an adaptation of Sicardy and Lissauer (1992).

Indeed, Lissauer (1985) proposed that two satellites could stabilize arcs, one maintaining particles at the L_4 and/or L_5 points, and another one providing the energy lost through collisions, confining radially the arc material thanks to the Lindblad resonances described in Section 5.5.1.2. This model predicts only one stable arc associated with the Lagrangian satellite. Despite the discovery of the satellite Galatea located ~ 980 km interior to the arcs, the images of the Voyager 2 mission, for which the maximal resolution was 12 km (Smith et al., 1989), did not reveal any co-orbital moon in the Adams ring.

Sicardy and Lissauer (1992) proposed a variant model by considering two co-orbital satellites at their mutual L_4 point, which allows the possible existence of satellites smaller than in the Lissauer (1985) model. However, the detailed geometry of Neptune's ring arcs (four arcs with different angular

lengths) is still unexplained with this model, requiring more sophisticated solutions.

5.5.3.1 Family of stable stationary configurations

Results on the existence of stationary configurations for co-orbital satellites with small and arbitrary masses were derived by Renner and Sicardy (2004).

Consider the circular planar restricted $1+N$ body problem with N co-orbital satellites moving with the same average mean motion n_0 (and orbital radius r_0) around a point mass M . In a coordinate system with origin at M and rotating with the velocity n_0 , the position of a satellite is described by the coordinates (ϕ_i, ξ_i) , $i = 1, \dots, N$, where ϕ_i is the longitude of satellite i with respect to an arbitrary origin, and $\xi_i = \Delta r_i/r_0$ is the relative radial excursion of that satellite. Choosing units such that $n_0 = r_0 = M = 1$, the equations of motion are then (see also Salo and Yoder (1988))

$$\begin{cases} \dot{\phi}_i = -\frac{3}{2}\xi_i \\ \dot{\xi}_i = -2 \sum_{j \neq i} m_j f'(\phi_i - \phi_j) \end{cases} \quad (5.13)$$

where

$$f(\phi) = \cos \phi - \frac{1}{2|\sin \phi/2|}, \quad (5.14)$$

In order to ensure that the satellites remain co-orbital, this system also assumes that any two satellites i and j never get closer than a few mutual Hill radii $r_H = r_0 \cdot [(m_i + m_j)/M]^{1/3}$. The first equation in (5.13) represents the differential keplerian velocity of each satellite with respect to r_0 , and the function $f(\phi)$ in Eq. (5.14) is the sum of the indirect and direct potentials exerted by a given satellite on the other co-orbital bodies. The fixed points of system (5.13) are given by:

$$\xi_i = 0 \quad (5.15)$$

and

$$\sum_{j \neq i} m_j f'(\phi_i - \phi_j) = 0 \quad (5.16)$$

for all $i = 1, \dots, N$. Eq. (5.15) means that in a stationary configuration the N co-orbital satellites have the same orbital radius. Eq. (5.16) involves the angular separations between the satellites and can be written in a matrix form. Defining $f'_{ij} \equiv f'(\phi_i - \phi_j)$ and noting that the function f' is odd, we obtain from Eq. (5.16):

$$\begin{bmatrix} 0 & f'_{12} & \cdots & \cdots & f'_{1N} \\ -f'_{12} & 0 & f'_{23} & \cdots & f'_{2N} \\ \vdots & & 0 & & \\ \vdots & & & \ddots & \\ -f'_{1N} & & & & 0 \end{bmatrix} \cdot \begin{bmatrix} m_1 \\ m_2 \\ \vdots \\ \vdots \\ m_N \end{bmatrix} = 0_{\mathbb{R}^N} \quad (5.17)$$

² The resonance argument is $\Psi_{CER} = 43\lambda - 42\lambda_G - \varpi_G$.

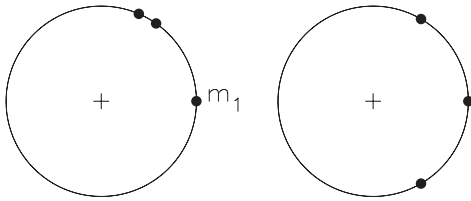


Figure 5.10 Stable stationary configurations for $N = 3$ co-orbital satellites with $m_2 = m_3 = 10^{-2}m_1$. From left to right, the angular separations of satellites 2 and 3 with respect to satellite 1 are: $(\phi_2, \phi_3) = (54^\circ.84, 66^\circ.75)$, $(59^\circ.82, 300^\circ.18)$. (Figure from Renner and Sicardy (2004))

Since the matrix M above is antisymmetric, its rank is even. Consequently, for given arbitrary angles ϕ_i 's, the existence of non-trivial solutions (positive or not) of the linear system (Eq. 5.17) depends on the parity of the number N of satellites. If N is odd, then there always exists a set of mass values that achieves stationarity for any arbitrary angular separation between the satellites. However, strictly positive masses restrict this existence to sub-domains of angular separations. If N is even, the rank of M is generally N , and there is in general no family of mass vectors that leads to a stationary configuration. This is well known for the case $N = 2$, where only the triangular points L_4 and L_5 and the diametral point L_3 allow the satellites to be stationary with respect to each other. Thus, one must first cancel the determinant of the matrix, $\det(M)$, in order to obtain non-trivial solutions of (Eq. 5.17).

Renner and Sicardy (2004) showed that the case $N = 3$ can be completely treated analytically for small arbitrary satellite masses, giving all the possible solutions and their linear stability. For $N \geq 4$, the possible stable stationary configurations for given satellite masses are derived following a numerical approach where the satellites converge towards the linearly stable equilibria, by adding a non-conservative term which brings energy in the equations of motion. Integrating these perturbed equations and exploring random initial coordinates with random masses then provides the domains of stable stationary points. These domains correspond to configurations where the co-orbitals are either positioned near the L_4 and L_5 points of the most massive satellite, or are grouped near one of these two points, as shown in the example displayed in Fig. 5.10.

5.5.3.2 Application to observations

Renner et al. (2014) demonstrated how the observed inter-arc regions lead to a limited space of possible mass ratios between hypothetical co-orbital satellites, achieving equilibrium. They applied the method above to $N = 4$ satellites (where the satellite $i = 1$ is by convention the most massive) with random initial mass ratios m_i/m_1 ($i = 2, 3, 4$) lower than three percent³, and stored the stable solutions with angular separations satisfying $\Phi_{32} = 11 \pm 3^\circ$, $\Phi_{43} = 12.5 \pm 3^\circ$

³ Increasing this value increases the average relative angular positions of the solutions, which could lead to configurations incompatible with the observed inter-arc regions.

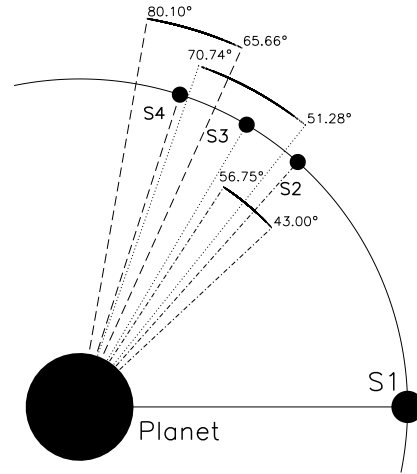


Figure 5.11 Subset of stationary configurations for $N = 4$ satellites, akin to the Lagrangian L_4/L_5 points. The mass ratios m_i/m_1 of the satellites S_i ($i = 2, 3, 4$) with respect to the most massive S_1 are lower than 0.03, and the angular separations are compatible with the observed inter-arc regions (see text). The satellites in equilibrium are close to the L_4/L_5 point of $S_1:S_2$ at a longitude with respect to S_1 between 43 and 56.75° , S_3 between 51.28 and 70.74° and S_4 between 65.66 and 80.1° . (Figure from Renner et al. (2014))

and $\Phi_{42} = 23.5 \pm 3^\circ$ (where Φ_{ij} is the azimuthal separation between the satellites i and j), that is, configurations compatible with the observed inter-arc regions (Porco, 1991; Dumas et al., 2002; de Pater et al., 2005). A continuum of mass values is obtained, with angular configurations where the co-orbitals are near the L_4 (or L_5) point of the most massive satellite, as illustrated in Fig. 5.11. Full numerical integrations then confirmed that the system is numerically stable under the effects of the perturbations due to the satellite Galatea. These perturbations are mainly the 42:43 LER and the 42:43 CIR, located about 0.25 km inside the arcs' semimajor axis. The moonlets have a slow libration motion around the stationary configuration, and arc particles are strongly maintained between the co-orbital satellites on much longer time scales than the observation time span of ~ 30 years.

5.5.4 Energy and angular momentum transfer

As mentioned earlier, the m (resp. $2m$) stable equilibria distributed around the orbit of a corotation resonance are at potential maxima. Thus, the energy dissipated by interparticle collisions must be replenished for an arc to remain confined. In general, a LER tends to exert a repulsive torque Γ on the arc particle, i.e. it tends to pull apart the particles and the satellites, independently of the detailed physics at play in the ring⁴ (Goldreich and Tremaine, 1980; Meyer-Vernet

⁴ This *standard* torque can be written

$$\Gamma = 0.4a^2n^2 \left(\frac{M_S}{M_P}\right)^2 \left(\frac{a}{a - a_S}\right)^4 M_r, \quad (5.18)$$

where M_r is the mass of the ring.

and Sicardy, 1987). Thus, arcs orbiting outside a satellite ($m < 0$) should gain angular momentum (and thus orbital energy), while arcs orbiting inside ($m > 0$) should lose orbital energy. Naively, one may thus expect that only arcs orbiting outside a satellite can be maintained. Things are more subtle, though, because a *differential* torque must in fact be exerted between the inner and the outer edges of the arc for stabilizing it. If we place ourselves in the frame corotating with the arcs, and if we denote ζ the potential energy (per unit mass) associated with the corotation resonance, then change rate $\dot{\zeta}$ for particles around corotation points, averaged over one libration period T_C , is

$$\dot{\zeta} = -\frac{3n_S}{4\pi\sigma a_0^2} \frac{1}{T_C} \int_{T_C} a \frac{d\Gamma}{da} dt, \quad (5.19)$$

where a_0 is the average orbital radius, σ the ring surface density, and $d\Gamma/da$ the torque density, that is, the torque exerted by the satellite per unit radius (Sicardy et al., 1991). Because of the presence of the term a in front of $d\Gamma/da$, the energy received is proportional to the gradient $d^2\Gamma/da^2$ of the torque density. Physically, this means that a given particle must undergo a larger repulsion on the inner side of its libration path than on the outer side, in order to compensate for the spreading effect due to dissipation. Thus, the resulting differential torque across a corotation site can serve to stabilize particles and form a stable ring arc.

Sicardy and Lissauer (1992) noticed that most of the energy supplied to the arcs is used to excite the eccentricities, not to confine the particles, assuming that the standard torque formula holds. Assuming that a stationary state is reached, the orbital migration of the Adams ring is approximately 3 km/yr, a value too high to stabilize the ring on long time scales. However, the standard torque formula may not be applicable for Neptune’s arcs since it assumes that Lindblad resonances $m+1 : m$ overlap, whereas the radial separation between two resonances is ~ 25 km, i.e. larger than the physical width of the ring.

5.5.5 Collisions

The most critical problem for the arc stability is the inelastic collisions between particles. In the framework of the CIR model with Galatea, Foryta and Sicardy (1996) noticed that the forced eccentricity gradient due to the Lindblad resonance implies potential collisions with typical relative velocities of about 1 m.s^{-1} , which can cause semimajor axis changes of about 10 km. Impacts between macroscopic particles, necessary to reproduce the observed dust ratios, break the resonance capture with the satellite over short time scales, as confirmed by numerical collisional N-body simulations (Hänninen and Porco, 1997). Salo and Hänninen (1998) then considered self-gravity between macroscopic co-orbital particles (with radii in the range 0.1-1 km) to effectively reduce the collision frequency and thus stabilize the arcs in CIR with Galatea. The equations (5.13), coupled with the CIR equations, were used to find that a few kilometer-sized particles can be maintained in resonance without colliding with each other. In this model, the kilometer-sized bodies separate the arc into different segments, which explains

partly the observed azimuthal lengths, while sub-kilometer particles supply dust in the ring and account for the clumpy structure of the arcs.

5.6 Summary, Conclusions, and Outlook

Although much progress has been made on characterizing and understanding Neptune’s ring system, including its ring arcs, our knowledge is clearly hampered by the scarcity of good data, which by itself is not surprising as the rings and ring arcs are very faint. Since the Voyager flybys, several data sets have been obtained with HST, Keck and the VLT; some of these data have been shown in this review chapter, but clearly much work remains to be done. The data reduction and analysis, including careful photometry, of these data is tedious and time consuming. In the future, with the next generation of large, 30–40 m, ground-based telescopes and JWST, the sensitivity to Neptune’s rings and ring arcs will be much improved. But rather than waiting for these telescopes, it remains important during the intervening years to continue observing the ongoing evolution of the ring arcs; perhaps new arcs may form. The physics of confining these arcs, and the original formation of the arcs can only be determined if a database of the evolution of the ring arcs is established.

In addition to the ring arcs, it is also crucial to regularly observe Neptune’s small moons, as the interaction between moons and ring arcs is clearly important to understand the physics. Based upon observations taken so far, it is clear that the orbits of Neptune’s moons are not well-characterized by the Voyager data, and one new inner moon has been discovered since then (Showalter et al., 2013a).

5.6.1 Origin

The origin of the arc system could be the breakup of a parent satellite or the accretion of ring material within the Roche zone of the planet. The latter is outside the Adams ring for a density of 1 g cm^{-3} (Esposito, 2002), allowing a mixture of collisional rings and accreted moonlets. The Galatea secular torque (Section 5.5.4) could help to set a few ring moonlets in stable stationary configurations, provided that the energy generated by the Lindblad resonance is higher than that dissipated through collisions. The exact origin of the proposed configuration of co-orbital bodies is still unknown. Such a mechanism could be hierarchical if accretion plays a significant role: a (previously accreted) satellite could gather some ring material around its L_4 or L_5 Lagrangian point, then larger co-orbital particles would form close to L_4/L_5 until a stationary configuration is reached. The ring arcs observed would be the residual material confined in between these small satellites. Simulations of self-gravitating and colliding particles (see, e.g., Rein and Liu (2012)) need to be performed to study the formation mechanisms of small satellites close to the Roche zone of a planet. Once the system of co-orbital bodies is in a stationary configuration, the secular

torque and therefore the ring orbital migration are reduced (Sicardy and Lissauer, 1992).

5.6.2 Dynamical evolution

The dynamical evolution of Neptune’s partial rings is unknown: the existence of a system of small co-orbital satellites might be part of an incomplete process of satellite formation. Alternatively, Neptune’s arcs could be transitory, resulting in a new ring if the equilibrium configuration breaks down. The latest Keck and HST observations show that the leading two arcs (Courage, Liberté) appear to have vanished, while the trailing two (Egalité, Fraternité) appear to have remained quite stable. Though it seems they must be submitted to confinement mechanisms, the arcs nevertheless evolve rapidly.

Acknowledgements

I.d.P. acknowledges partial support from NSF grant 1615004. M.R.S. acknowledges support from NASA’s Outer Planets Research Program through grant NNX14AO40G, and from Space Telescope Science Institute through program HST-GO-14217. Support for Program number HST-GO-14217 was provided by NASA through a grant from the Space Telescope Science Institute, which is operated by the Association of Universities for Research in Astronomy, Incorporated, under NASA contract NAS5-26555. B.S. acknowledges funding from the French grant ”Beyond Neptune II” (ANR-11-IS56-0002) and from the European Research Council under the European Community’s H2020 (2014-2020/ ERC Grant Agreement no. 669416 ”LUCKY STAR”).

REFERENCES

- de Pater, I., and Lissauer, J. J. 2015. *Planetary Sciences*. Cambridge Univ. Press.
- de Pater, I., Showalter, M. R., Burns, J. A., Nicholson, P. D., Liu, M. C., Hamilton, D. P., and Graham, J. R. 1999. Keck Infrared Observations of Jupiter’s Ring System near Earth’s 1997 Ring Plane Crossing. *Icarus*, **138**, 214–223.
- de Pater, I., Martin, S. C., and Showalter, M. R. 2004. Keck near-infrared observations of Saturn’s E and G rings during Earth’s ring plane crossing in August 1995. *Icarus*, **172**, 446–454.
- de Pater, I., Gibbard, S. G., Chiang, E., Hammel, H. B., Macintosh, B., Marchis, F., Martin, S. C., Roe, H. G., and Showalter, M. 2005. The dynamic neptunian ring arcs: evidence for a gradual disappearance of Liberté and resonant jump of courage. *Icarus*, **174**, 263–272.
- de Pater, I., Hammel, H. B., Gibbard, S. G., and Showalter, M. R. 2006. New Dust Belts of Uranus: One Ring, Two Ring, Red Ring, Blue Ring. *Science*, **312**, 92–94.
- Dumas, C., Terrile, R. J., Smith, B. A., Schneider, G., and Becklin, E. E. 1999. Stability of Neptune’s ring arcs in question. *Nature*, **400**, 733–735.
- Dumas, C., Terrile, R. J., Smith, B. A., and Schneider, G. 2002. Astrometry and Near-Infrared Photometry of Neptune’s Inner Satellites and Ring Arcs. *AJ*, **123**, 1776–1783.
- El Moutamid, M., Sicardy, B., and Renner, S. 2014. Coupling between corotation and Lindblad resonances in the presence of secular precession rates. *Celestial Dynamics and Dynamical Astronomy*, **118**, 235–252.
- Esposito, L. W. 2002. Planetary rings. *Reports on Progress in Physics*, **65**, 1741–1783.
- Foryta, D. W., and Sicardy, B. 1996. The Dynamics of the Neptunian ADAMS Ring’s Arcs. *Icarus*, **123**, 129–167.
- Goldreich, P., and Tremaine, S. 1980. Disk-satellite interactions. *Astrophysical Journal*, **241**, 425–441.
- Goldreich, P., Tremaine, S., and Borderies, N. 1986. Towards a theory for Neptune’s arc rings. *AJ*, **92**, 490–494.
- Hänninen, J., and Porco, C. 1997. Collisional Simulations of Neptune’s Ring Arcs. *Icarus*, **126**, 1–27.
- Hubbard, W. B. 1986. 1981N1 - A Neptune arc? *Science*, **231**, 1276–1278.
- Hubbard, W. B., Brahic, A., Sicardy, B., Elicer, L.-R., Roques, F., and Vilas, F. 1986. Occultation detection of a Neptunian ring-like arc. *Nature*, **319**, 636–640.
- Jacobson, R. A. 2009. The Orbits of the Neptunian Satellites and the Orientation of the Pole of Neptune. *Astron. J.*, **137**(May), 4322–4329.
- Jacobson, R. A., and Owen, Jr., W. M. 2004. The Orbits of the Inner Neptunian Satellites from Voyager, Earth-based, and Hubble Space Telescope Observations. *Astron. J.*, **128**(Sept.), 1412–1417.
- Karkoschka, E. 2003. Sizes, shapes, and albedos of the inner satellites of Neptune. *Icarus*, **162**, 400–407.
- Lissauer, J. J. 1985. Shepherding model for Neptune’s arc ring. *Nature*, **318**, 544.
- Manfroid, J., Haefner, R., and Bouchet, P. 1986. New evidence for a ring around Neptune. *Astron. Astrophys.*, **157**, L3–L5.
- Meyer-Vernet, N., and Sicardy, B. 1987. On the physics of resonant disk-satellite interaction. *Icarus*, **69**, 157–175.
- Murray, C. D., and Dermott, S. F. 2000. *Solar System Dynamics*. Cambridge Univ. Press.
- Namouni, F., and Porco, C. 2002. The confinement of Neptune’s ring arcs by the moon Galatea. *Nature*, **417**, 45–47.
- Nicholson, P. D., Cooke, M. L., Matthews, K., Elias, J. H., and Gilmore, G. 1990. Five stellar occultations by Neptune - Further observations of ring arcs. *Icarus*, **87**, 1–39.
- Nicholson, P. D., Mosqueira, I., and Matthews, K. 1995. Stellar occultation observations of Neptune’s rings: 1984–1988. *Icarus*, **113**, 295–330.
- Owen, W. M., Vaughan, R. M., and Synnott, S. P. 1991. Orbits of the six new satellites of Neptune. *Astronomical Journal*, **101**, 1511–1515.
- Porco, C. C. 1991. An explanation for Neptune’s ring arcs. *Science*, **253**, 995–1001.
- Porco, C. C., Nicholson, P. D., Cuzzi, J. N., Lissauer, J. J., and Esposito, L. W. 1995. Neptunes ring system. In: Cruikshank, D. P., Matthews, M. S., and Schumann, A. M. (eds.), *Neptune and Triton*. University of Arizona Press. Pages 703–804.
- Rein, H., and Liu, S.-F. 2012. REBOUND: an open-source multi-purpose N-body code for collisional dynamics. *Astronomy and Astrophysics*, **537**, A128.
- Renner, S., and Sicardy, B. 2004. Stationary Configurations for Co-orbital Satellites with Small Arbitrary Masses. *Celestial Mechanics and Dynamical Astronomy*, **88**, 397–414.
- Renner, S., Sicardy, B., Souami, D., Carry, B., and Dumas, C. 2014. Neptune’s ring arcs: VLT/NACO near-infrared observations and a model to explain their stability. *Astron. Astrophys.*, **563**, A133.
- Salo, H., and Hänninen, J. 1998. Neptune’s Partial Rings: Action of Galatea on Self-Gravitating Arc Particles. *Science*, **282**, 1102–1104.
- Salo, H., and Yoder, C. F. 1988. The dynamics of coorbital satellite systems. *Astronomy and Astrophysics*, **205**, 309–327.
- Showalter, M. R., and Cuzzi, J. N. 1992. Physical Properties of Neptune’s Ring System. *AAS/Division for Planetary Sciences Meeting Abstracts*, **24**, 1029.
- Showalter, M. R., Lissauer, J. J., and de Pater, I. 2005 (Aug.). The Rings of Neptune and Uranus in the Hubble Space Telescope. *AAS/Division for Planetary Sciences Meeting Abstracts*, **37**, 772.

- Showalter, M. R., de Pater, I., Lissauer, J. J., and French, R. S. 2013a. New Satellite of Neptune: S/2004 N 1. *Central Bureau Electronic Telegrams*, **3586**(July).
- Showalter, M. R., de Pater, I., French, R. S., and Lissauer, J. J. 2013b. The Neptune System Revisited: New Results on Moons and Rings from the Hubble Space Telescope. *AAS/Division for Planetary Sciences Meeting Abstracts*, **45**, 206.01.
- Showalter, M. R., de Pater, I., Lissauer, J. J., and French, R. S. 2016 (Oct.). Hubble Observations of the Ongoing Evolution of Neptune's Ring-Moon System. *AAS/Division for Planetary Sciences Meeting Abstracts*, **48**, 203.09.
- Sicardy, B., and Lissauer, J. J. 1992. Dynamical models of the arcs in Neptune's 63K ring (1989N1R). *Advances in Space Research*, **12**, 81–95.
- Sicardy, B., Roques, F., and Brahic, A. 1991. Neptune's rings, 1983–1989: Ground-based stellar occultation observations. I - Ring-like arc detections. *Icarus*, **89**, 220–243.
- Sicardy, B., Roddier, F., Roddier, C., Perozzi, E., Graves, J. E., Guyon, O., and Northcott, M. J. 1999. Images of Neptune's ring arcs obtained by a ground-based telescope. *Nature*, **400**, 731–733.
- Smith, B. A., Soderblom, L. A., Banfield, D., Barnett, C., Basilevsky, A. T., Beebe, R. F., Bollinger, K., Boyce, J. M., Brahic, A., Briggs, G. A., Brown, R. H., Chyba, C., Collins, S. A., Colvin, T., Cook, A. F., Crisp, D., Croft, S. K., Cruikshank, D., Cuzzi, J. N., Danielson, G. E., Davies, M. E., de Jong, E., Dones, L., Godfrey, D., Goguen, J., Grenier, I., Haemmerle, V. R., Hammel, H., Hansen, C. J., Helfenstein, C. P., Howell, C., Hunt, G. E., Ingersoll, A. P., Johnson, T. V., Kargel, J., Kirk, R., Kuehn, D. I., Limaye, S., Marsursky, H., McEwen, A., Morrison, D., Owen, T., Owen, W., Pollack, J. B., Porco, C. C., Rages, K., Rogers, P., Rudy, D., Sagan, C., Schwartz, J., Shoemaker, E. M., Showalter, M., Sicardy, B., Simonelli, D., Spencer, J., Sromovsky, L. A., Stoker, C., Strom, R. G., Suomi, V. E., Synott, S. P., Ter-rile, R. J., Thomas, P., Thompson, W. R., Verbiscer, A., and Veverka, J. 1989. Voyager 2 at Neptune: Imaging Science Results. *Science*, **246**, 1422–1449.
- Thomas, P., and Veverka, J. 1991. Neptune's small inner satellites. *J. Geophys. Res.*, **96**, 19261.